

## Research Article

# Dynamic Modeling and Improved Control of a Grid-Connected DFIG Used in Wind Energy Conversion Systems

**Abdeslam Jabal Laafou** , **Abdessalam Ait Madi**, **Adnane Addaim**,  
and **Abdessamad Intidam**

*National School of Applied Sciences, Ibn Tofail University, Kenitra, Morocco*

Correspondence should be addressed to Abdeslam Jabal Laafou; [abdeslam.jaballaafou@uit.ac.ma](mailto:abdeslam.jaballaafou@uit.ac.ma)

Received 5 April 2020; Revised 26 May 2020; Accepted 5 June 2020; Published 23 July 2020

Academic Editor: Libor Pekař

Copyright © 2020 Abdeslam Jabal Laafou et al. This is an open access article distributed under the Creative Commons Attribution License, which permits unrestricted use, distribution, and reproduction in any medium, provided the original work is properly cited.

The proposed work presented in this paper is mainly focused on the control of the active and reactive stator powers generated by a wind energy conversion system (WECS) based on the dual feed induction generator (DFIG). This control is achieved by acting on the rotor side converter (RSC) to extract the maximum power from the wind turbine (WT) while regulating the rotor currents. Furthermore, another control objective is achieved by acting on the grid side converter (GSC), in which the DC bus voltage is maintained constant and a unity power factor is ensured. To do that, a new robust control known as active disturbance rejection control (ADRC) has been proposed and applied to the WECS. This control is based on the extended state observer (ESO), which is the main core of this algorithm; it makes the estimation and cancellation of the total effect of various uncertainties (internal and external disturbances) possible in real time. To validate the effectiveness of the proposed approach, the system was modeled and simulated by using the Matlab/Simulink software. Two tests, namely, tracking and robustness tests, were performed to compare the proposed ADRC technique and classical PI controllers. The obtained results are promising and have shown that the proposed control strategy based on ADRC, especially when varying the mode parameters, is performant and very useful.

## 1. Introduction

Both population growth and industrialization during these recent decades, especially in emerging countries, have led to a significant increase in global demand for electrical energy [1]. In addition, the cost of energy continues to increase due to the scarcity of nonrenewable resources used in the supply of power generation plants. Renewable energies are a particularly suitable response to the considerable energy needs of the planet, which could increase by 50% or more by 2030 [2].

Among these renewable energies, we find green wind energy, which is one of the sustainable and renewable energy solutions for the production of electrical energy [3]. One major issue affecting these kinds of energy resources is the wind speed, which can change quickly, especially during gusts. These speed variations generate significant mechanical stresses on the system, which are more reduced with the use

of an asynchronous machine than with a synchronous generator, which operates at fixed speed. That is why today the use of variable speed wind turbines is increasing compared to the fixed-speed wind turbines.

The use of a dual feed induction generator (DFIG) is one solution proposed in the literature, for variable speed wind turbine structures. Several reasons have led to the use of this DFIG; the first one is that these machines are known by their robustness and their reduced efforts on mechanical parts, and the second one is their possibility for active and reactive control power. On the other hand, the use of the back-to-back converters to connect the generator rotor to the grid allows the transit of a fraction of the total system power. Consequently, the cost and losses in the components of power electronics converters are then reduced [4].

In the literature, to obtain a decoupled control of the active and reactive powers of the DFIG, the authors [5] have proposed the use of the oriented stator tension vector

control when the authors [6] have proposed the use of the oriented stator flux vector control. The control of active and reactive power is obtained with a controller named rotor current regulator [7], direct torque control (DTC) [8], or modified direct power control (MDPC) [9]. However, the wind turbine system (WTS) is a complex system with nonlinearities, strong coupling, multiple variables, signal wind energy, which are random, and time, which is varying, and disturbance of the system parameters caused by the disturbance of the external environment. These issues make it difficult to obtain the accurate mathematical model, which brought great challenges to the initial design [10]. Therefore, for these characteristics of the WTS, designing more detailed and comprehensive control methods to solve these disturbance and nonlinear problems is of great significance for the safe and reliable operation of the WTS and also achieving maximum power tracking. At present, few research studies have been presented [5–7] using proportional integral (PI) regulators and oriented stator flux control for controlling the rotor current. But the problem while using the PI regulator is the parameters tuning and its robustness to DFIG parameter variations. Some authors have looked for other power control options for DFIG using the rotor current vector loop like the functional predictive controller [11], the internal model controller [12], the model predictive control [13], the sliding mode control [14, 15], or feedback linearization control [16]. These controllers are designed using the DFIG model and have a satisfactory power response compared to the power response of the PI, although they are barely implemented due to the complex formulations of the controllers. Another possibility for power control can be done by using artificial intelligence (AI) approaches such as fuzzy logic (FL) and neural networks (NN) [17]. These strategies are designed by system knowledge and have a satisfactory power response, although they present expensive implementations in terms of high calculation, uncertainty due to knowledge of system parameters, and variations can lead to a degradation of system performance. In order to overcome the shortcomings of the classical linear PID control, Jingqing Han has proposed a new controller known as the active disturbance rejection control (ADRC) [18].

The ADRC extracts the disturbance information directly from the input and output signals of the controlled object by the means of an extended state observer (ESO) and eliminates the disturbance by the final control amount; the disturbance signal is cancelled before it is applied to the output signal [18]. At present, the ADRC control strategy has been widely used in various fields such as machinery production, power systems, and process control, and it has been highly praised by researchers at worldwide [19–23]. This disruption rejection command allows the user to treat the system being studied as a simpler model, as the negative effects of external disturbances and modeling uncertainties are compensated in real time.

In this context, this paper investigates the control ADRC of the grid connected wind conversion system based on DFIG, in order to deal with the system complexity and its uncertainties. Principally, the main contribution of this

work lies on the design and development of the new robust control strategy by the use of the ADRC for the grid connected WECS based on DFIG. This approach ensures the maximum power capture available from the wind and controls the power delivery. Therefore, the ADRC is used to control the RSC, GSC, direct current (DC), and active and reactive powers.

For this purpose, the present paper is organized as follows: the first section treats the general introduction; the second presents the overall architecture of the proposed system and the modeling of its components. The third section introduces the mathematical theory and design of the ADRC strategy. The fourth section illustrates the application of the proposed control by ADRC for the overall conversion system, and in the fifth section, the simulation results and discussion are presented.

## 2. Modeling of the Wind Energy Conversion System

In this section, the modeling of the elements of the WECS is shown, going from the conversion of wind kinetic energy into mechanical energy to the connection with the electrical grid. Based on physics laws and neglecting the mechanical and electrical losses that are assumed to have no effect on the dynamic behavior of the system, a dynamic model of each element of WECS is established. The WECS is illustrated in Figure 1. Its components are as follows:

- (i) Three-bladed, horizontal axis wind turbine
- (ii) Gearbox system that adapts the turbine low rotational speed to the speed required by the generator
- (iii) DFIG with nominal power of 1.5 MW
- (iv) Two bidirectional converters (RSC and GSC) interconnected via a DC bus
- (v) Three-phase filter and a step-up transformer

**2.1. Wind Turbine Modeling.** The WT is a rotating device that converts a part of the wind kinetic power into a mechanical power at the turbine rotor [24], or the aerodynamic wind power available on a surface  $S$  swept by the turbine blades is expressed by the derivation of the kinetic energy of the air mass passing through this surface, as shown by

$$P_w = \frac{1}{2} \rho S V^3, \quad (1)$$

where  $\rho$ : the air density ( $\approx 1.22 \text{ kg/m}^3$ ),  $S = \pi R^2$ : the swept area by the blades of the radius turbine  $R$ , and  $V$ : the wind speed (m/s).

According to the Betz law [13, 14], the turbine recovers only a fraction of this power  $P_w$ ; or each wind turbine is defined by its own power coefficient  $C_p(\lambda, \beta)$ . This power coefficient represents the aerodynamic efficiency of the WT, which depends on the geometric characteristics of the blades, the pitch angle  $\beta$  and the speed ratio  $\lambda$  [12]. As a result, the captured aerodynamic power is given by

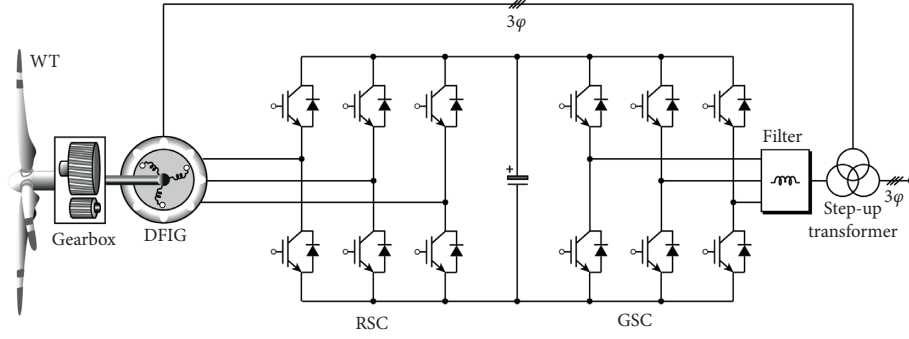


FIGURE 1: Schematic diagram of wind turbine based on DFIG.

$$P_t = C_p(\lambda, \beta)P_w = \frac{1}{2}C_p(\lambda, \beta)\rho\pi R^2V^3. \quad (2)$$

The mechanical torque appearing on the turbine rotor can therefore be subsequently represented by

$$T_t = \frac{1}{2 \cdot \Omega_t} C_p(\lambda, \beta) \rho \pi R^2 V^3, \quad (3)$$

where  $\Omega_t$  is the turbine speed.

The power coefficient is most often presented as a nonlinear function of  $\lambda$  and  $\beta$  and whose theoretical upper limit is given by Betz's law [13, 14]. In this article,  $C_p(\lambda, \beta)$  is expressed by the following function:

$$C_p(\lambda, \beta) = 0.5176 \left( \frac{116}{\lambda'} - 0.4\beta - 5 \right) e^{-21/\lambda'} + 0.0068\lambda, \quad (4)$$

with

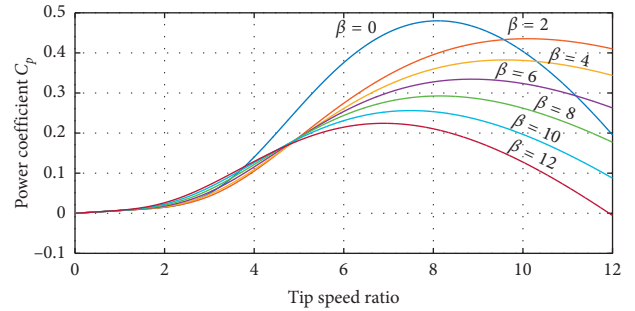
$$\frac{1}{\lambda_i} = \frac{1}{\lambda + 0,08\beta} + \frac{0,035}{1 + \beta^3}, \quad (5)$$

$$\lambda = \frac{\Omega_t \cdot R}{V}. \quad (6)$$

Figure 2 shows the evolution of the power coefficient  $C_p(\lambda, \beta)$  as a function of  $\lambda$  for different values of  $\beta$ . It can be observed that when the pitch angle  $\beta$  increases, the coefficient  $C_p$  decreases, which results in a reduction in the wind kinetic energy captured by the turbine.

**2.2. Gearbox and Mechanical Shaft Modeling.** The gearbox, which connects the slow shaft of the turbine to the fast shaft that drives the generator, aims to adapt the turbine speed to that required by the generator [24]. The gearbox used generally includes two or three epicyclic gear trains to obtain high multiplication ratios (from  $\approx 50$  to  $\approx 100$ ). It is modeled using a torque and speed gain  $G$  corresponding to the multiplication ratio:

$$\begin{cases} \Omega_t = \frac{1}{G} \Omega_m, \\ T_m = \frac{1}{G} T_t. \end{cases} \quad (7)$$


 FIGURE 2: Evolution of the power coefficient according to  $\lambda$  and  $\beta$ .

The total inertia of the system consisting of the WT and the generator is expressed by equation (8) (the inertia of the turbine is transferred to the generator rotor):

$$J = \frac{J_t}{G^2} + J_g. \quad (8)$$

Consequently, the mechanical shaft model is presented by

$$J \frac{d\Omega_m}{dt} = T_m - T_{em} - f\Omega_m, \quad (9)$$

where  $\Omega_m$  is the generator rotor speed,  $J$  is the total inertia,  $J_g$  the DFIG inertia,  $J_t$  is the turbine inertia,  $T_m$  the torque applied to the shaft of the generator,  $T_{em}$  is the electromagnetic torque produced by the generator, and  $f\Omega_m$  represents the torque of viscous friction.

**2.3. DFIG Modeling with Stator Flux Orientation.** The DFIG consists of a three-phase stator directly connected to the grid and a rotor formed by the three-phase windings accessible by three rings equipped with sliding contacts and connected to the grid via a two-stage power electronics converter [14]. In the literature, several modeling methods have been discussed, although the most commonly used model for DFIG is the Park model [13], which allows to write a dynamic model in a direct quadrature (DQ) reference frame as follows:

The electrical equations are given by

$$\left\{ \begin{array}{l} V_{sd} = R_s i_{sd} + \frac{d\phi_{sd}}{dt} - \omega_s \phi_{sq}, \\ V_{sq} = R_s i_{sq} + \frac{d\phi_{sq}}{dt} + \omega_s \phi_{sd}, \\ V_{rd} = R_r i_{rd} + \frac{d\phi_{rd}}{dt} - \omega_r \phi_{rq}, \\ V_{rq} = R_r i_{rq} + \frac{d\phi_{rq}}{dt} + \omega_r \phi_{rd}. \end{array} \right. \quad (10)$$

$$\left\{ \begin{array}{l} V_{sd} = R_s i_{sd} + \frac{d\phi_{sd}}{dt} = 0, \\ V_{sq} = \omega_s \phi_s, \\ V_{rd} = R_r i_{rd} + L_r \sigma \frac{di_{rd}}{dt} - g\omega_s L_r \sigma i_{rq}, \\ V_{rq} = R_r i_{rq} + L_r \sigma \frac{di_{rq}}{dt} - g\omega_s L_r \sigma i_{rd} + g\omega_s \frac{V_s L_m}{L_s \omega_s}. \end{array} \right. \quad (14)$$

The stator and rotor flux are shown by

$$\left\{ \begin{array}{l} \phi_{sd} = L_s i_{sd} + L_m i_{rd}, \\ \phi_{sq} = L_s i_{sq} + L_m i_{rq}, \\ \phi_{rd} = L_r i_{rd} + L_m i_{sd}, \\ \phi_{rq} = L_r i_{rq} + L_m i_{sq}. \end{array} \right. \quad (11)$$

The electromagnetic torque  $T_{em}$  is written as

$$T_{em} = \frac{3}{2} p \frac{L_m}{L_s} (\phi_{sq} i_{rd} - \phi_{sd} i_{rq}). \quad (12)$$

The active and reactive stator and rotor powers are given in  $dq$  reference frame by

$$\left\{ \begin{array}{l} P_s = \frac{3}{2} (V_{sd} i_{sd} + V_{sq} i_{sq}), \\ Q_s = \frac{3}{2} (V_{sq} i_{sd} - V_{sd} i_{sq}), \\ P_r = \frac{3}{2} (V_{rd} i_{rd} + V_{rq} i_{rq}), \\ Q_r = \frac{3}{2} (V_{rq} i_{rd} - V_{rd} i_{rq}), \end{array} \right. \quad (13)$$

where  $v_{sd}$  and  $v_{sq}$ ,  $v_{rd}$  and  $v_{rq}$ ,  $i_{sd}$  and  $i_{sq}$ ,  $i_{rd}$  and  $i_{rq}$ ,  $\psi_{sd}$  and  $\psi_{sq}$ ,  $\psi_{rd}$  and  $\psi_{rq}$  are the direct and quadrature components of stator voltages, rotor voltages, stator currents, rotor currents, stator flux, and rotor flux in the DQ reference frame.  $R_s$  and  $R_r$  are the stator and rotor resistances,  $L_s$  and  $L_r$  are the stator and rotor inductances,  $L_m$  is the mutual inductance,  $\omega_s$  and  $\omega_r$  are the stator and rotor pulsations speed, and  $p$  is the poles pair number [21].

In order to simplify the control of the active and reactive powers, and to achieve the vector control of the DFIG, an orientation of the stator flux is required. In this article, the stator field vector is oriented along the d-axis; hence,  $\phi_{sd} = \phi_s$  and  $\phi_{sq} = 0$  [25].

Assuming that the stator resistance  $R_s$  is negligible and that the stator flux is constant, the DFIG equations become as follows:

Rotor and stator voltages are

Active and reactive stator powers are

$$\left\{ \begin{array}{l} P_s = -\frac{3}{2} \frac{V_s L_m}{L_s} i_{rq}, \\ Q_s = \frac{3}{2} \left( \frac{V_s \phi_s}{L_s} - \frac{V_s L_m}{L_s} i_{rd} \right). \end{array} \right. \quad (15)$$

Electromagnetic torque is

$$T_{em} = -\frac{3}{2} p \frac{L_m}{L_s} \phi_s i_{rq}, \quad (16)$$

where  $\sigma = (1 - L_m^2/L_r L_s)$  is the dispersion coefficient.

**2.4. Back-to-Back Converters Modeling.** The WECS studied in this work transfers a portion of its power to the grid by means of two-stage power converter coupled on a common DC bus; these converters are bidirectional and controlled by pulse width modulation (PWM). In this work, both converters are identical and can be used in both inverter and rectifier modes. Figure 3 illustrates the simplified model of the GSC, filter, and grid. The converter consists of controllable components (e.g., insulated gate bipolar transistor (IGBT)) connected with antiparallel diodes allowing the bidirectional circulation of current [26].

Each transistor-diode set is considered as a perfect switch  $T_{ij}$ , and every switch state is quantized by a connection function  $s_{ij}$  given by

$$s_{ij} = \begin{cases} 1, & \text{if } T_{ij} \text{ ON,} \\ 0, & \text{if } T_{ij} \text{ OFF,} \end{cases} \quad (17)$$

with  $i = 1, 2$  and  $j = 1, 2, 3$ .

The switches states are complementary:

$$s_{1j} + s_{2j} = 1, \quad \forall j \in \{1, 2, 3\}. \quad (18)$$

The modulated voltages are expressed by

$$\begin{aligned} v_{f-a} &= \frac{2s_{11} - (s_{12} + s_{13})}{3} U_{dc}, \\ v_{f-b} &= \frac{2s_{12} - (s_{11} + s_{13})}{3} U_{dc}, \\ v_{f-c} &= \frac{2s_{13} - (s_{11} + s_{12})}{3} U_{dc}. \end{aligned} \quad (19)$$

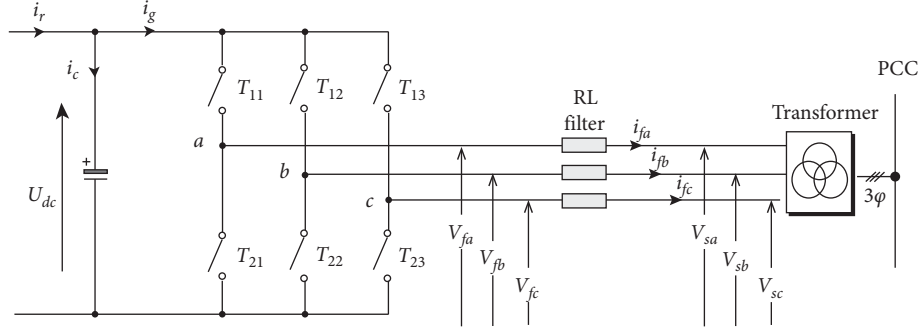


FIGURE 3: Simplified model of the GSC, filter, and grid.

The modulated current  $I_{inv}$  is given by

$$I_{inv} = s_{11}i_{f-a} + s_{12}i_{f-b} + s_{13}i_{f-c}. \quad (20)$$

Applying Park's transformation, equations (19) and (20) become as follows:

$$\begin{aligned} v_{fd} &= s_d U_{dc}, \\ v_{fq} &= s_q U_{dc}, \\ I_{inv} &= s_d i_{fd} + s_q i_{fq}, \end{aligned} \quad (21)$$

where  $v_{fd}$  and  $v_{fq}$  are the inverter voltages,  $i_{fd}$  and  $i_{fq}$  are the grid filter currents,  $U_{dc}$  is the DC bus voltage, and  $s_d$  and  $s_q$  are the switches state in DQ reference frame.

**2.5. DC Link and Filter Modeling.** The connection with the electrical grid by means of rotor side is carried out via a filter ( $L_f, R_f$ ) [26]:

$$\begin{aligned} v_{s-a} &= v_{f-a} - R_f i_{f-a} - L_f \frac{di_{f-a}}{dt}, \\ v_{s-b} &= v_{f-b} - R_f i_{f-b} - L_f \frac{di_{f-b}}{dt}, \\ v_{s-c} &= v_{f-c} - R_f i_{f-c} - L_f \frac{di_{f-c}}{dt}. \end{aligned} \quad (22)$$

Equation (22) becomes in DQ frame as follows:

$$\begin{aligned} v_{sd} &= v_{fd} - R_f i_{fd} - L_f \frac{di_{fd}}{dt} + L_f \omega_s i_{fq}, \\ v_{sq} &= v_{fq} - R_f i_{fq} - L_f \frac{di_{fq}}{dt} - L_f \omega_s i_{fd}, \end{aligned} \quad (23)$$

where  $v_{sd}$  and  $v_{sq}$  are the grid voltages.

The modeling of DC Link Voltage is given by

$$\frac{dU_{dc}}{dt} = \frac{1}{C} (i_r - i_g), \quad (24)$$

with  $C$  being the DC link Capacitor and  $i_r, i_g$  being, respectively, the currents modulated by the RSC and the GSC.

### 3. Structure and Principle of ADRC

The ADRC control strategy is robust control method proposed by Jinging HAN [18] to overcome the deficiencies of the conventional control by PID [21]. To illustrate the principle of the ADRC technique, let us consider a single-input, single-output nonlinear time-varying controlled object [24]:

$$\begin{cases} \dot{x}^n = f(x, \dot{x}, \dots, x^{n-1}, w, t) + b \cdot u, \\ x = y, \end{cases} \quad (25)$$

where:  $x, \dot{x}, \dots, x^n$  respectively represents the object state and its various order dynamics,  $w$  is the external disturbances,  $f(x, \dot{x}, \dots, x^{n-1}, w, t)$  represents all internal and external (total) disturbances affecting the system to be controlled,  $u$  and  $y$  are the system input and output, respectively, and  $b$  is the control gain.

In engineering practice, it is often difficult to accurately establish and determine the system dynamic model and control gain. There are various uncertainties; because of this, model-based control theory and methods have encountered great difficulties and challenges in engineering practice [19]. The advantage of ADRC is that even if the dynamic model of the system is not clear, and there is a large uncertainty in the control gain, good control performance can still be obtained. The basic structure of the ADRC controller is shown by the block diagram in Figure 4. It includes three parts: the tracking differentiator (TD), the ESO, and the state error feedback (SEF) control law. These three parts can have many different forms. For the difference, if each part of the ADRC contains a nonlinear link, it is called nonlinear ADRC; otherwise, if they are designed as linear links, they are called linear ADRCs [19]. The principles of the three parts are introduced below. Among them,  $b_0$  can be an approximate estimated constant value of  $b$ , which can also be adjusted according to the control needs and can also be adaptive online.

**3.1. Tracking Differentiator (TD).** The purpose of the TD is to arrange the transition process and then reduce the initial error, which affects the system in the initial stage, by effectively resolving the contradiction between overshoot and fastness. It can be achieved by TD or an appropriate function

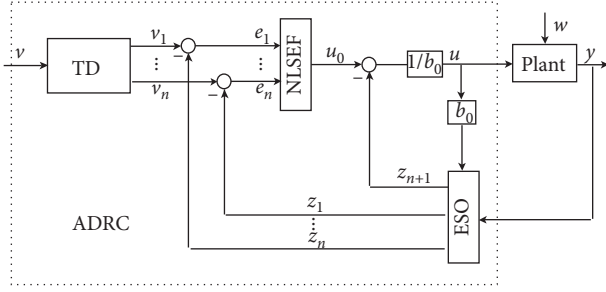


FIGURE 4: Block diagram of n order nonlinear ADRC.

generator. TD was originally used to track the input signal as quickly as possible, while giving an approximate differential signal. At present, TD is often used to arrange the transition process, so the form of TD is mainly introduced here.

The general form of a continuous nonlinear tracking differentiator is shown in [19] and given by

$$\begin{cases} \dot{v}_1 = v_2, \\ \dot{v}_2 = v_3, \\ \vdots \\ \dot{v}_n = r^n f\left(v_1 - v, \frac{v_2}{r}, \dots, \frac{v_n}{r^{n-1}}\right), \end{cases} \quad (26)$$

where  $v$  is the TD input signal,  $v_i$  ( $i = 1, 2, \dots, n$ ) is the TD output signal,  $v_1$  is the tracking signal of the input  $v$ , and  $v_i$  ( $i = 1, 2, \dots, n$ ) is the  $(i-1)$  order differential of  $v_1$ , which can be approximated as  $(i-1)$  order differentiation;  $r$  is called the speed factor, and the larger  $r$  is, the faster  $v_1$  tracks the input signal  $v$ .

**3.2. Extended State Observer (ESO).** In this stage, it is assumed that the dynamic model of the system is completely unknown, and the “total disturbance”  $f(\cdot)$  is estimated online and in real time through the extended state assuming that  $x_1 = x, \dots, x_n = x^{n-1}$ ; let  $x_{n+1} = f(\cdot)$  be the extended state variables of the system, then the general form of designing a continuous extended state observer is shown in [19] and expressed by

$$\begin{cases} e = z_1 - y, \\ \dot{z}_1 = z_2 - \beta_{01} \cdot g_1(e), \\ \dot{z}_2 = z_3 - \beta_{02} \cdot g_2(e), \\ \vdots \\ \dot{z}_n = z_{n+1} - \beta_{0n} \cdot g_n(e) + b_0 \cdot u, \\ \dot{z}_{n+1} = -\beta_{0(n+1)} \cdot g_{n+1}(e), \end{cases} \quad (27)$$

where  $z_i$  ( $i = 1, 2, \dots, n+1$ ) are the estimated values of states  $x_i$  ( $i = 1, 2, \dots, n$ ) and  $x_{n+1} = f(\cdot)$  the total disturbances;  $\beta_{0i}$  ( $i = 1, 2, \dots, n+1$ ) is the observer adjustable gains, and  $g_n(e)$  ( $i = 1, 2, \dots, n+1$ ) is a nonlinear constructed function.

Under certain conditions, ESO can estimate the state of the object and the total disturbance of the system with a certain accuracy; that is,

$$z_1 \longrightarrow x_1, \dots, z_n \longrightarrow x_n, z_{n+1} \longrightarrow f(\cdot). \quad (28)$$

For the specific design of ESO, a large number of existing observer and filter design techniques can be used for the specific form of ESO. Han Jingqing [18] chose  $g_i(e)$  as the specific nonlinear function, which has the form mentioned in [21] by

$$g_i(e) = \text{fal}(e, a_i, \delta) = \begin{cases} |e|^{a_i} \text{sgn}(e), & |e| > \delta, \\ \frac{e}{\delta^{1-a_i}}, & |e| \leq \delta, \end{cases} \quad (29)$$

where  $0 < a_i < 1$ , and  $\delta > 0$  are adjustable parameters; when  $a_i = 1$ ,  $g_i(e) = e$ , that is, the traditional Luenberger observer, also known as linear ESO.

**3.3. State Error Feedback Control Law.** ESO obtains the estimated value of the total disturbance in real time. If it is compensated in the control law, the function of active disturbance rejection can be realized. Therefore, the control law is taken as shown in [20], given by

$$u = \frac{u_0 - z_{n+1}}{b_0}, \quad (30)$$

where  $u_0$  is the initial control component. If the estimation error of  $z_{n+1}$  on the unknown total disturbance “ $f(\cdot) + (b - b_0)u$ ” is ignored, then the object defined by the equation (25) is converted into a “series of integrators” as follows:

$$x^n = f(\cdot) + (b - b_0)u - z_{n+1} + u_0 \approx u_0. \quad (31)$$

In this way, the controlled objects that are full of disturbances, uncertainties, and nonlinearities are uniformly converted into standard integrators types, which turns the design of the control system from complex to simple, from abstract to intuitive, and having broad applicability.

The control component  $u_0$  has multiple implementations [21], and here is a general Nonlinear SEF (NLSEF) control law for controlled objects of any order:

$$u_0 = \sum_{i=1}^n k_i \text{fal}(e_i, a'_i, \delta'), \quad (32)$$

where  $e_i = v_i - z_i$ ,  $k_i$  is the gain coefficient, and  $a'_i$  and  $\delta'$  are undetermined constants, usually chosen as  $0 < a_i < 1 < a'_i$  ( $i = 1, 2, \dots, n$ ). In this way, the differential effect will become smaller when it is close to the steady state, which will help improve the performance of the control system [21].

When  $a'_i = 1$  ( $i = 1, 2, \dots, n$ ), the control law becomes linear. The advantage of linear control law is that the parameter tuning is simple and the control effect is relatively smooth.

**3.4. Linear ADRC Design.** In practice, the nonlinear ADRC has a large number of parameters that need to be adjusted, and adjusting them is a very hard and complicated task. As a result, in order to reduce the model complexity and the controller computational, a linear ADRC design method is

proposed. In the proposed structure, the TD block is omitted and the standard Luenberger observer with state expansion is used as the linear ESO to estimate the system states and the generalized disturbance; the NLSEF controller is replaced by a proportional controller that drives the tracking error between the system output and reference signal to zero. Figure 5 shows the block diagram of a first-order linear ADRC [26].

Consider a first-order plant where the plant dynamics is given by

$$\begin{cases} \dot{x} = -\frac{1}{T}x + b \cdot u, \\ x = y. \end{cases} \quad (33)$$

An external disturbance  $d$  is added to the system and modeling errors are taken into account by means of  $\Delta b$  ( $b = b_0 + \Delta b$ ). Then the system is rewritten by equation (34) as shown in [26]:

$$\dot{y} = -\frac{1}{T}y + w + \Delta b \cdot u + b_0 \cdot u = f(y, w, t) + b_0 u = f(\cdot) + b_0 u. \quad (34)$$

Let  $x_1 = y$ ,  $x_2 = f$ , and  $\dot{f} = h$ .

The system state-space model is given then by

$$\begin{cases} \dot{x} = Ax + Bu + Eh, \\ y = Cx. \end{cases} \quad (35)$$

where

$$\begin{aligned} A &= \begin{bmatrix} 0 & 1 \\ 0 & 0 \end{bmatrix}, \\ B &= \begin{bmatrix} b \\ 0 \end{bmatrix}, \\ C &= [1 \ 0], \\ E &= \begin{bmatrix} 0 \\ 1 \end{bmatrix}, \\ x &= \begin{bmatrix} x_1 \\ x_2 \end{bmatrix}. \end{aligned} \quad (36)$$

The linear ESO (LESO), presented in Figure 6, is designed as  $a_i = 1$ ; therefore, the corresponding observer is presented by

$$\begin{cases} \dot{z} = Az + Bu + K(y - \hat{y}), \\ \hat{y} = Cz, \end{cases} \quad (37)$$

where  $z$  is the observed states vector,  $z = [z_1 \ z_2]^T$  ( $z_1$  is the estimation of  $x_1$  and  $z_2$  is the estimation of  $x_2$ ),  $\hat{y}$  is the estimated output, and  $K$  is the observer gain vector.

Vector  $K$  is defined by

$$K = [\beta_{01} \ \beta_{02}]^T = [2\omega_0 \ \omega_0^2]^T, \quad (38)$$

where  $\omega_0$  is determined by the poles placement in closed-loop to ensure both fast observer dynamics and minimal perturbations sensitivity [26].

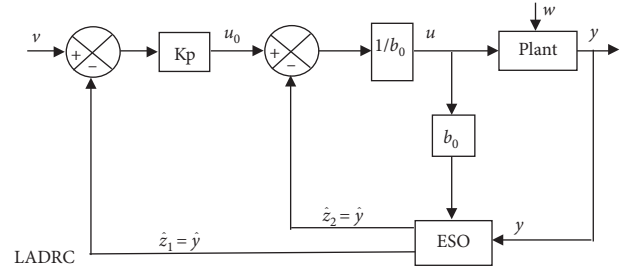


FIGURE 5: First-order linear ADRC block diagram.

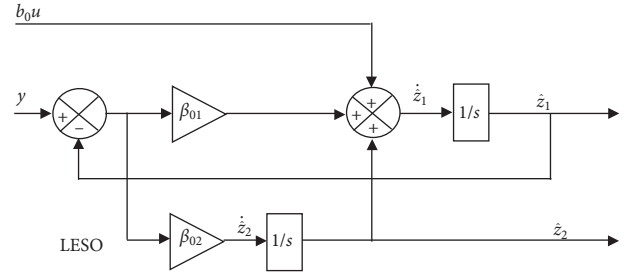


FIGURE 6: First-order linear extended state observer.

As mentioned in the previous section, if  $a'_i = 1$ , the control law by ADRC is set as a linear controller. According to [26], first-order plant equation (33) becomes

$$u_0 = k_p. \quad (39)$$

As a result, a proportional controller is used to control system (34):

$$u_0 = k_p(v - z_1) = k_p(v - \hat{y}). \quad (40)$$

The controller tuning is chosen as  $k_1 = \omega_c = 4/T_{\text{settle}}$  where  $T_{\text{settle}}$  is the desired closed loop settling time. The dynamics of the ESO must be fast compared to that of the controller. Therefore, the poles of the observer are placed to the left of the system closed-loop poles. In this case,  $\omega_0$  is selected as  $\omega_0 = 3 \sim 10 \omega_c$ .

#### 4. DFIG Wind Turbine Control by ADRC

After having modeled the different elements of the wind conversion chain based on the DFIG, this section discusses the control strategy by ADRC of the DFIG through the two power electronics converters with three main objectives:

- (i) Maximum power extraction by optimal torque control
- (ii) A decoupled control of the active and reactive stator powers by controlling the rotor side converter with ADRC approach
- (iii) DC bus voltage control and unit power factor ensuring by acting on the grid-side converter using the ADRC approach

**4.1. Maximum Power Point Tracking (MPPT).** The most successful control strategy for WTs directly connected to the power grid is based on the MPPT technique [27]. The

principle of this technique is to rotate the turbine over a certain wind speed range in order to maintain the tip speed ratio (TSR)  $\lambda$  at its optimal value  $\lambda_{\text{opt}}$  which makes the turbine operating at  $C_p = C_{p_{\text{max}}}$ .

Consider equation (6). The captured power from the wind is expressed as a function of the rotational speed  $\omega_m$ :

$$P_t = 0.5\rho\pi R^5 \frac{C_p(\lambda, \beta)}{\lambda^3} \omega_m^3. \quad (41)$$

Replacing  $\lambda$  by  $\lambda_{\text{opt}}$  and replacing  $C_p(\lambda, \beta) = C_{p_{\text{max}}}$ , the maximum power to be captured is expressed by

$$P_{t_{\text{max}}} = K_{\text{opt}} \omega_m^3, \quad (42)$$

where  $K_{\text{opt}}$  is a coefficient:

$$K_{\text{opt}} = 0.5\rho\pi R^5 \frac{C_{p_{\text{max}}}(\lambda_{\text{opt}}, \beta)}{\lambda_{\text{opt}}^3}. \quad (43)$$

Therefore, the reference electromagnetic torque for adjusting the rotational speed in order to extract the maximum power from the wind is given by

$$T_{em\_ref} = K_{\text{opt}} \omega_m^2. \quad (44)$$

**4.2. Rotor Side Converter Control by ADRC.** The main objective in this stage is to regulate the transfer of the stator active and reactive powers to the power grid [25]. The control is ensured by the regulation of rotor currents, where the direct component  $I_{rd}$  ensures the control of the reactive power, and the quadrature component  $I_{rq}$  controls either the active power to its desired reference or the electromagnetic torque to ensure the MPPT. The corresponding control is illustrated in Figure 7.

From equation (16), we deduce the reference current  $i_{rq\_ref}$  given by equation (45) allowing the electromagnetic torque produced by the DFIG to be regulated to its reference value imposed by the MPPT strategy:

$$i_{rq\_ref} = -\frac{2}{3} \frac{L_s}{pL_m\psi_s} T_{em\_ref} = -\frac{2}{3} \frac{L_s}{pL_m\psi_s} K_{\text{opt}} \omega_m^2. \quad (45)$$

Similarly, the reference rotor current  $i_{rd\_ref}$  shown by equation (46) is determined, from equation (15), in order to control the reactive power supplied or absorbed by the generator:

$$i_{rd\_ref} = \frac{2}{3} \left( \frac{\psi_s}{L_m} - \frac{L_s}{v_s L_m} \right) Q_{s\_ref}. \quad (46)$$

The rotor currents  $i_{rd}$  and  $i_{rq}$  are controlled by two ADRC type regulators as shown in Figure 7.

The knowledge of the stator flux  $\psi_s$  is necessary for the design of this control; it can be estimated from measurements of the direct component of the stator and rotor currents (equation (11)). For the synthesis of the ADRC controllers, the last two equations from equation (14) are rewritten to express the dynamics of the rotor currents:

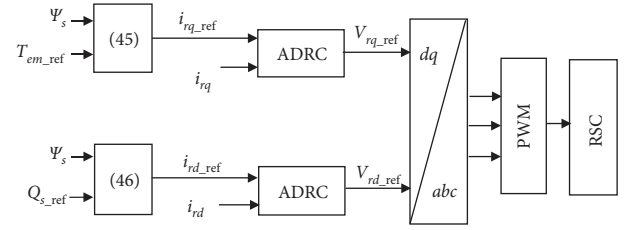


FIGURE 7: Control of the RSC by ADRC.

$$\frac{di_{rd}}{dt} = -\frac{R_r}{\sigma L_r} i_{rd} + \omega_r i_{rq} + \frac{1}{\sigma L_r} v_{rd}, \quad (47)$$

$$\frac{di_{rq}}{dt} = -\frac{R_r}{\sigma L_r} i_{rq} - \omega_r i_{rd} - \omega_r \frac{L_m}{\sigma L_s L_r} \psi_s + \frac{1}{\sigma L_r} v_{rq}. \quad (48)$$

These expressions can be written in the canonical form of an ADRC controller given by

$$\frac{di_{rd}}{dt} = f_d(\cdot) + b_{r0} u_d, \quad (49)$$

where

$$\begin{cases} f_d(\cdot) = -\frac{R_r}{\sigma L_r} i_{rd} + \omega_r i_{rq} + \left( \frac{1}{\sigma L_r} - b_{r0} \right) v_{rd}, \\ b_{r0} = \frac{1}{\sigma L_r}; \\ u_d = v_{rd}. \end{cases} \quad (50)$$

In addition,

$$\frac{di_{rq}}{dt} = f_q(\cdot) + b_{r0} u_q, \quad (51)$$

where

$$\begin{cases} f_q(\cdot) = -\frac{R_r}{\sigma L_r} i_{rq} - \omega_r i_{rd} - \omega_r \frac{L_m}{\sigma L_s L_r} \psi_s + \left( \frac{1}{\sigma L_r} - b_{r0} \right) v_{rq}, \\ b_{r0} = \frac{1}{\sigma L_r}; \\ u_q = v_{rq}, \end{cases} \quad (52)$$

where  $f_d(\cdot)$  and  $f_q(\cdot)$  represent the total disturbances affecting the currents  $i_{rd}$  and  $i_{rq}$ , respectively.  $b_{r0}$  is the known part of the generator parameters.

**4.3. Grid Side Converter Control by ADRC.** The control of this converter makes it possible to control the currents flowing in the filter ( $R_f, L_f$ ) in order to keep the DC bus voltage constant regardless of the power exchanged between the DFIG and the power grid, and to ensure the control the active and reactive powers flowing through the connection point. The power factor can be kept unitary by imposing a

zero reactive power reference. The block diagram of the adopted control strategy is shown in Figure 8. It involves a dual-loop control structure: an outer dc-link voltage control loop and an inner current control loop.

As mentioned before the grid voltages are oriented such that  $v_{sd} = 0$  and  $v_{sq} = V_s$ . As a result, equations 24 are re-written by using

$$\frac{di_{fd}}{dt} = -\frac{R_f}{L_f}i_{fd} - \omega_s i_{fq} - \frac{1}{L_f}v_{fd}, \quad (53)$$

$$\frac{di_{fq}}{dt} = -\frac{R_f}{L_f}i_{fq} + \frac{1}{L_f}V_s - \omega_s i_{fd} - \frac{1}{L_f}v_{fq}. \quad (54)$$

The active and reactive powers exchanged with the power grid through the filter are expressed by

$$P_f = \frac{3}{2}V_s i_{fq}, \quad (55)$$

$$Q_f = \frac{3}{2}V_s i_{fd}. \quad (56)$$

The power across the DC link Capacitor C can be expressed by

$$P_{dc} = U_{dc}(i_g - i_r). \quad (57)$$

And we have

$$\frac{dU_{dc}}{dt} = \frac{1}{C}(i_g - i_r), \quad (58)$$

or

$$P_{dc} = CU_{dc} \frac{dU_{dc}}{dt}. \quad (59)$$

By neglecting all the losses in filter, power electronics converters, and the capacitor, the exchanged power on the DC bus is given by

$$P_{dc} = P_f - P_r, \quad (60)$$

where  $P_r, P_f$  are the generator rotor side and filter side powers, respectively.

By taking into account equations (55)–(60), the DC bus voltage is expressed by using

$$CU_{dc} \frac{dU_{dc}}{dt} = \frac{3}{2}V_s i_{fq} - U_{dc} i_r, \quad (61)$$

or

$$\frac{dU_{dc}^2}{dt} = \frac{3V_s}{C}i_{fq} - \frac{2U_{dc}}{C}i_r. \quad (62)$$

We put  $X = U_{dc}^2$ ; then, we have

$$\frac{dX}{dt} = \frac{3V_s}{C}i_{fq} - \frac{2\sqrt{X}}{C}i_r. \quad (63)$$

Therefore, we obtain the canonical form of the ADRC controller such that

$$\frac{dX}{dt} = f_X(\cdot) + b_{c0}u_X, \quad (64)$$

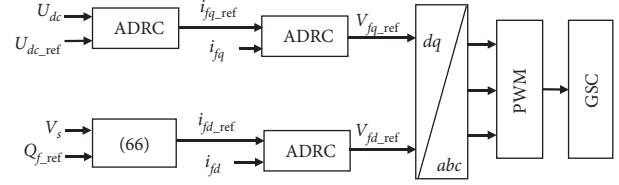


FIGURE 8: Control of GSC by ADRC.

or

$$\begin{cases} f_X(\cdot) = -\frac{2\sqrt{X}}{C}i_r + \left(\frac{3V_s}{C} - b_{c0}\right)i_{fq}, \\ b_{c0} = \frac{3V_s}{C}; \\ u_X = i_{fq}. \end{cases} \quad (65)$$

The external voltage regulation loop makes it possible to maintain the voltage across the capacitor  $U_{dc}$  constant and to generate the reference current  $i_{fq\_ref}$  for the current inner loop [25]. The reference current  $i_{fd\_ref}$ , given by equation (66), is calculated by the desired delivery of reactive power:

$$i_{fd\_ref} = \frac{2}{3V_s}Q_{f\_ref}. \quad (66)$$

For the inner current control loop, equations (53) and (54) are adapted with the canonical forms of ADRC and then we obtain equations (67) and (69):

$$\frac{di_{fd}}{dt} = f_{fd}(\cdot) + b_{f0}u_{fd}, \quad (67)$$

with

$$\begin{cases} f_{fd}(\cdot) = \frac{R_f}{L_f}i_{fd} - \omega_s i_{fq} + \left(\frac{1}{L_f} - b_{f0}\right)V_{fd}, \\ b_{f0} = -\frac{1}{L_f}; \\ u_{fd} = V_{fd}. \end{cases} \quad (68)$$

In addition,

$$\frac{di_{fq}}{dt} = f_{fq}(\cdot) + b_{f0}u_{fq}, \quad (69)$$

with

$$\begin{cases} f_{fq}(\cdot) = \frac{1}{L_f}V_s - \frac{R_f}{L_f}i_{fq} - \omega_s i_{fd} + \left(\frac{1}{L_f} - b_{f0}\right)V_{fq}, \\ b_{f0} = -\frac{1}{L_f}; \\ u_{fq} = V_{fq}. \end{cases} \quad (70)$$

## 5. Simulations and Results

The DFIG based wind conversion system was modeled and simulated under the Matlab/Simulink environment. The WECS parameters used for the simulation are given in the Appendix section.

To illustrate the performance of the ADRC control strategy, two tests, namely, tracking and robustness tests, have been conducted under different conditions. It should be noted that, throughout the first test, the reference reactive powers  $Q_{s\_ref}$  and  $Q_{f\_ref}$  are set at zero, in order to ensure a unit power factor at the grid connection point, and in the second test, the stator reactive power reference has been set to  $Q_{s\_ref} = -1e^5$  VAR.

**5.1. Tracking Test.** In this test, a variable speed wind profile is applied to the WT blades, as illustrated in Figure 9, to validate tracking effectiveness of the proposed control strategy. The following wind speed profile corresponds, as shown in Figure 10, to a DFIG mechanical speed in MPPT control varying between 1200 rpm and 1750 rpm. The generator therefore operates in both hypynchronous and hypersynchronous modes with slip varying from -16, 6% to about 20%.

It can be observed from Figure 11 that the power coefficient  $C_p$  was maintained at its optimum value, which corresponds to the MPPT. The corresponding extracted power by the WT is shown in Figure 12.

Figures 13 and 14 show the regulation of the rotor currents  $i_{rd}$  and  $i_{rq}$  by PI and ADRC; it can be seen that both of them follow their references; however, the ADRC shows a better dynamic response and follows its references perfectly. Current  $i_{rq}$ , which controls the electromagnetic torque  $T_{em}$  of the generator, varies according to the wind speed profile so as to extract maximum power; this can be seen in Figure 15. Current  $i_{rd}$ , which controls the reactive power  $Q_s$ , is kept constant to have a unit power factor on the stator side as highlighted in Figure 16.

Figures 17 and 18 show the waveforms of the stator and rotor currents generated by the DFIG; it can be seen that stator currents follow the variation of the wind; on the other hand, the rotor currents show that the DFIG works in hypynchronous when the wind speed is less than 1500 rpm and in hypersynchronous when the wind speed is higher than 1500 rpm (2 s to 3.7 s).

Figure 19 shows that the DC bus voltage  $U_{dc}$  was kept constant by both regulators (ADRC and PI); however, the PI controllers present an overshoot of 250 V compared to the ADRC controller.

Figures 20–23 represent the simulation results of currents  $i_{fd}$  and  $i_{fq}$  of the (Rf, Lf) filter and the active and reactive powers exchanged with power via the rotor side.

Current  $i_{fd}$  tracks perfectly its zero setpoint, which allows having a reactive power zero on the grid side. Current  $i_{fq}$  was maintained at its set value, which allows the exchange of active power between the DFIG Rotor and the grid according to the wind profile.

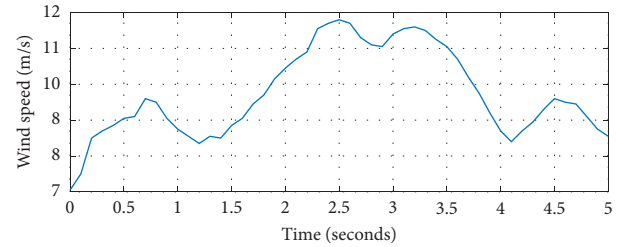


FIGURE 9: Applied variable wind speed profile.

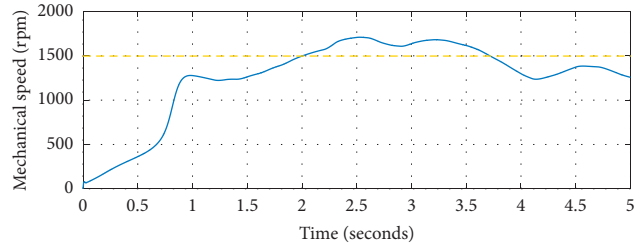


FIGURE 10: DFIG Mechanical speed (rpm).

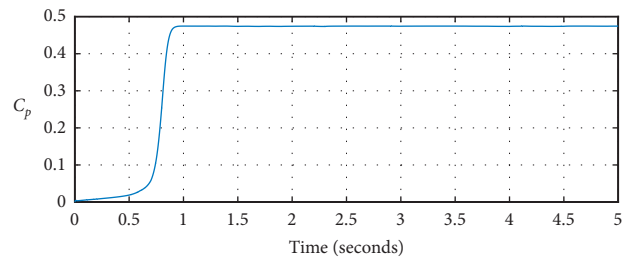


FIGURE 11: Turbine power coefficient.

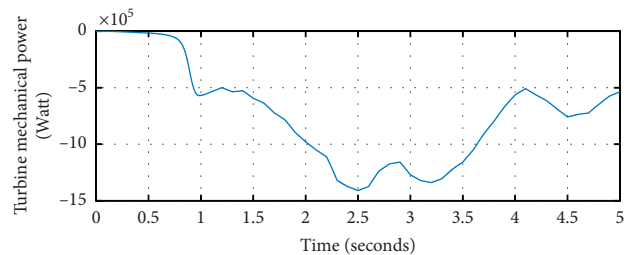


FIGURE 12: Extracted wind turbine mechanical power.

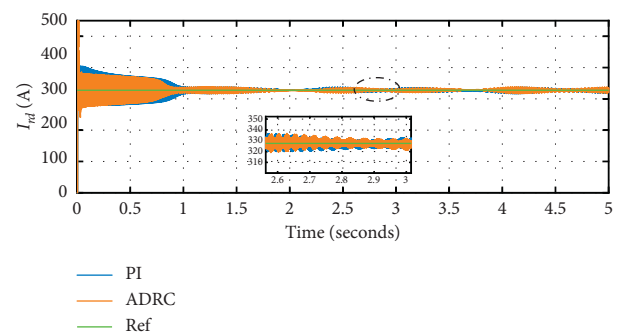


FIGURE 13: Regulation of the current  $i_{rd}$  by PI and ADRC.

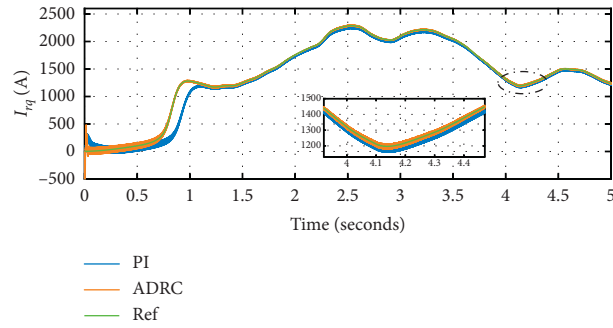


FIGURE 14: Regulation of the current  $i_{rq}$  by PI and ADRC.

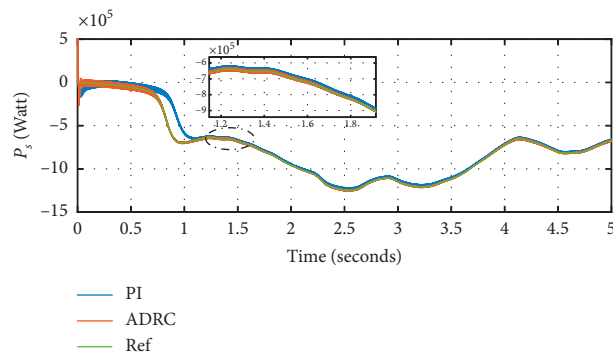


FIGURE 15: Active power regulation by PI and ADRC.

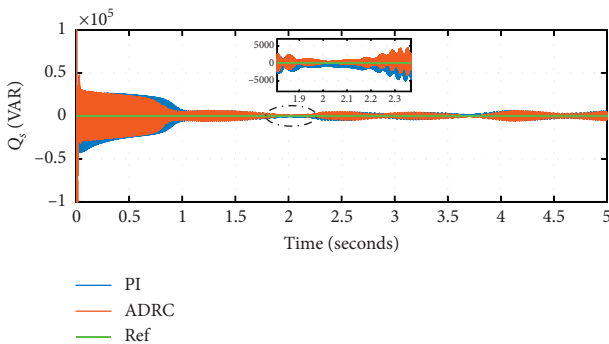


FIGURE 16: Reactive power regulation by PI and ADRC.

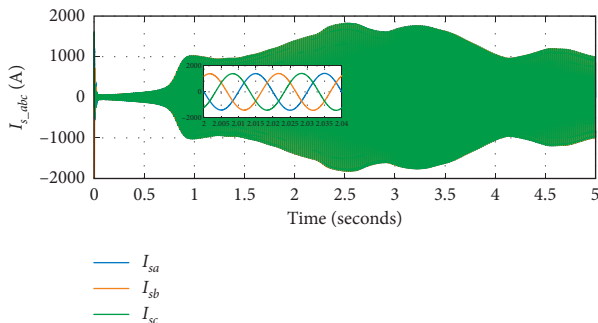


FIGURE 17: Waveforms of generated stator currents.

Figure 24 illustrates the waveforms of phase stator current  $i_{sa}$  and grid voltage  $v_{sa}$ ; it can be observed that the current and voltage are in phase opposition, which means zero reactive power injection and active power delivery to the grid.

**5.2. Robustness Test.** The robustness test consists in varying the DFIG model parameters. Indeed, the calculations of the regulators are based on functions whose parameters are assumed to be fixed. However, in a real system, these parameters are subject to variations caused by different physical phenomena. Figures 25–28 show the evolution of the active and reactive power injected by stator side or the image of the rotor currents regulation. During this test, the same wind speed profile was kept, and the reference of the stator reactive power was changed from zero to  $Q_{s\_ref} = -1e^5 VAR$  at  $t = 2.5$  and then returned to zero at  $t = 4$ . Two robustness tests were made; in the first one, the rotor resistance  $R_r$  was increased by 100%, and in the second one, the inductance  $L_r$  was changed by 30%.

As it can be concluded from the figures shown, these variations of  $R_r$  and  $L_r$  have almost no influence on the ADRC regulators, due to its capability in automatically estimating and compensating the disturbances by means of the ESO, which is not the case for the classical PI controller; its tuning gains are designed according to the model parameters, and this variation affects its performance compared to the ADRC.

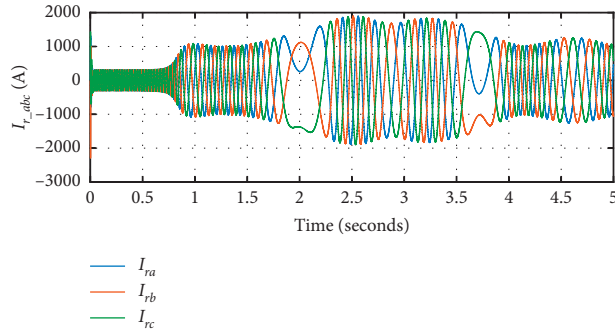


FIGURE 18: Waveforms of generated rotor currents.

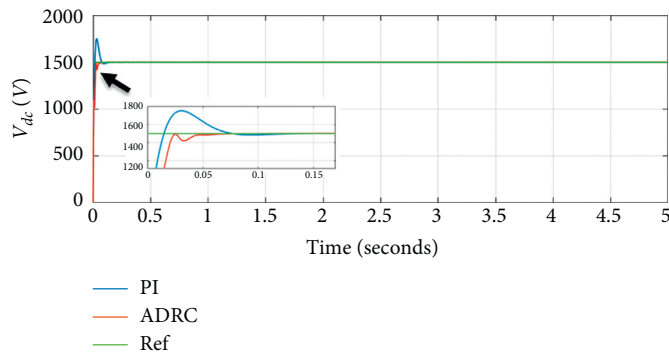


FIGURE 19: DC bus voltage regulation by ADRC and PI.

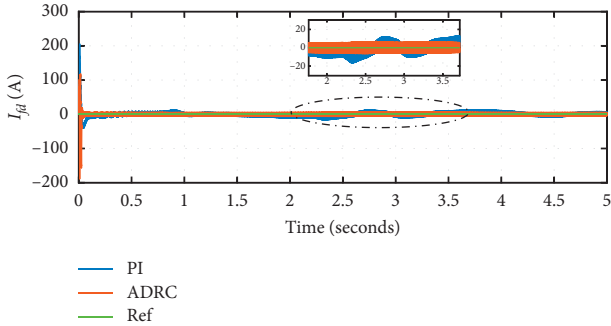


FIGURE 20: Regulation of the current  $i_{fd}$  by PI and ADRC.

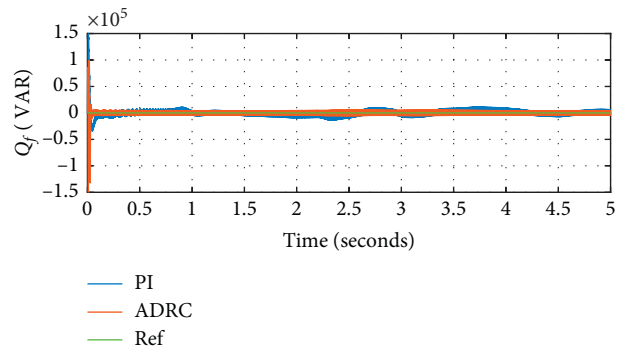


FIGURE 22: Reactive power regulation by PI and ADRC.

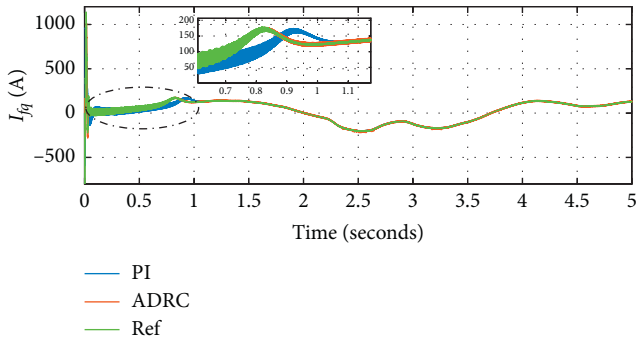


FIGURE 21: Regulation of the current  $i_{fq}$  by PI and ADRC.

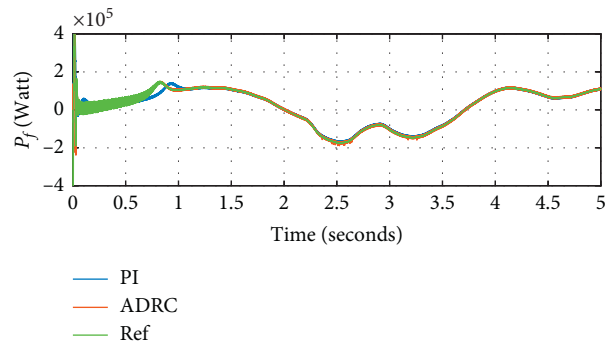


FIGURE 23: Active power regulation by PI and ADRC.

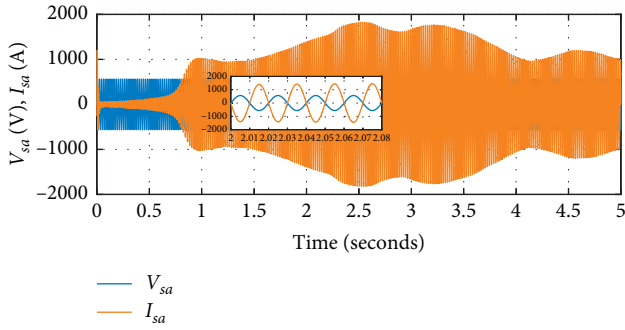


FIGURE 24: Waveforms of phase a stator  $i_{sa}$  current and grid voltage  $v_{sa}$ .

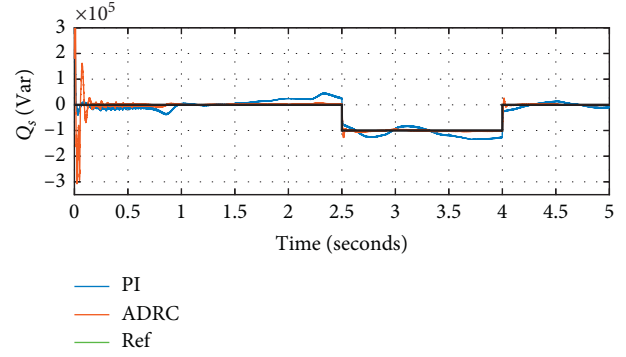


FIGURE 28: Stator reactive power regulation for  $1.3 * Lr$ .

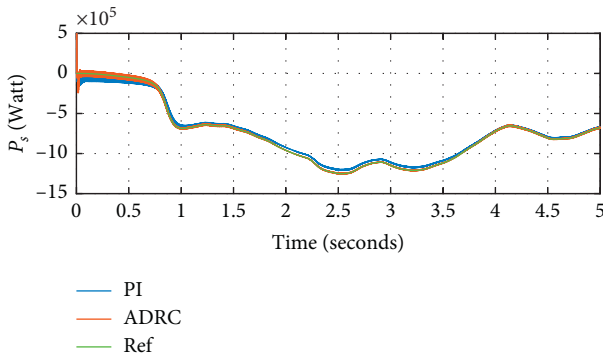


FIGURE 25: Stator Active power regulation for  $2 * Rr$ .

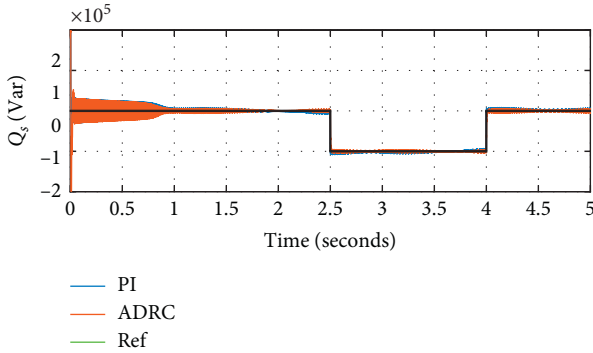


FIGURE 26: Stator Reactive power regulation for  $2 * Rr$ .

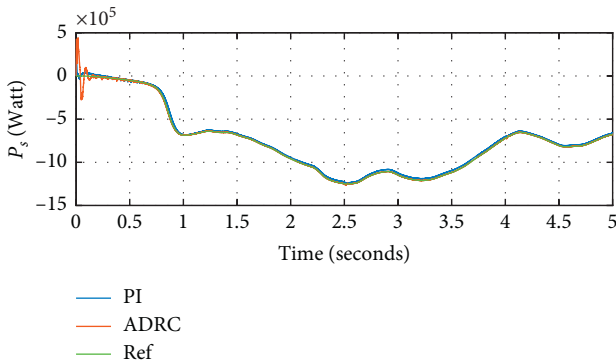


FIGURE 27: Stator Active power regulation for  $1.3 * Lr$ .

TABLE 1: The parameters of the DFIG.

Parameters	Values
The rated power $P_n$	1.5 MW
The rated voltage $U_n$	690 V
The nominal frequency	50 Hz
The rated rotor speed	1750 tr/min
The number of pole pairs	2
The stator resistance $R_s$	2.65 mΩ
The rotor resistance $R_r$	2.63 mΩ
The stator leakage inductance $L_{s\sigma}$	0.1687 mH
The rotor leakage inductance $L_{r\sigma}$	0.1337 mH
The magnetizing inductance $L_m$	5.4749 mH

TABLE 2: The parameters of the turbine.

The rated power	1.5 MW
The rated wind speed	13 m/s
Density of air	1.225 kg/m <sup>3</sup>
Blade radius	30 m
The gearbox ratio $G$	57

TABLE 3: The parameters of the grid side.

Parameters	Values
The DC-link voltage $U_{dc}$	1320 V
The DC-link capacitor $C$	10028.7 μF
The filter resistance $R_f$	0.3174 Ω
The filter inductance $L_f$	3.0103 mH

TABLE 4: ADRC parameters.

Parameters	Values
$K_p^r$	400
$\beta_{01}$	2400
$\beta_{02}$	1,440,000

TABLE 5: PI controller parameters.

	Parameters	Values
For the rotor currents	$K_p^r$	0.8921
	$K_i^r$	7.8900
For the grid currents	$K_p^g$	9.0309
	$K_i^g$	105.4380
For the DC link voltage	$K_p^{dc}$	1.0029
	$K_i^{dc}$	50.1586

## 6. Conclusion

This paper was devoted to the modeling and control of the variable speed wind energy conversion system based on the DFIG, where the main objective is to operate the WT so as to extract the maximum power from the wind energy. To reach this goal a control strategy based on ADRC regulators has been proposed and applied to control the RSC via the rotor currents, the GSC and DC bus voltage through the currents flowing in filter, and the active and reactive power transits between the WT and the electrical power grid.

To validate the effectiveness of the proposed system, the system was modeled and simulated under the Matlab/Simulink environment. Two tests, namely, tracking and robustness, were performed to compare the proposed ADRC technique and classical PI controllers. The obtained results are promising and have shown that the proposed control strategy based on ADRC, especially when varying the mode parameters, is very performant.

## Appendix

### Advice on Tables

The WECS parameters used for the simulation are given in Table 1 for the DFIG, Table 2 for the turbine, Table 3 for the grid side, Table 4 for the ADRC parameters, and for the PI controller parameters in Table 5.

## Data Availability

No data were used to support this study.

## Conflicts of Interest

The authors declare that they have no conflicts of interest.

## References

- [1] P. Nejat, F. Jomehzadeh, M. M. Taheri, M. Gohari, and M. Z. Abd Majid, "A global review of energy consumption, CO<sub>2</sub> emissions and policy in the residential sector (with an overview of the top ten CO<sub>2</sub> emitting countries)," *Renewable and Sustainable Energy Reviews*, vol. 43, pp. 843–862, 2015.
- [2] A. Pina, C. Silva, and P. Ferrão, "The impact of demand side management strategies in the penetration of renewable electricity," *Energy*, vol. 41, no. 1, pp. 128–137, 2012.
- [3] J. Jung and R. P. Broadwater, "Current status and future advances for wind speed and power forecasting," *Renewable and Sustainable Energy Reviews*, vol. 31, pp. 762–777, 2014.
- [4] T. R. Ayodele, A. A. Jimoh, J. L. Munda, and J. T. Agee, "Challenges of grid integration of wind power on power system grid integrity: a review," *World*, vol. 3, 2020.
- [5] D. Chwa and K.-B. Lee, "Variable structure control of the active and reactive powers for a DFIG in wind turbines," *IEEE Transactions on Industry Applications*, vol. 46, no. 6, pp. 2545–2555, 2010.
- [6] M. Arifujjaman, M. T. Iqbal, and J. E. Quaicoe, "Vector control of a DFIG based wind turbine," *Istanbul University-Journal of Electrical & Electronics Engineering*, vol. 9, no. 2, pp. 1057–1066, 2010.
- [7] F. Senani, A. Rahab, F. Louar, F. Bourourou, and H. Benalla, "Active and reactive power control of DFIG using PI and DPC controllers," in *Proceedings of the 2015 4th International Conference on Electrical Engineering (ICEE)*, IEEE, Boumerdes, Algeria, pp. 1–6, 2015.
- [8] Y. S. Rao and A. J. Laxmi, "Direct torque control of doubly fed induction generator based wind turbine under voltage dips," *International Journal of Advances in Engineering & Technology*, vol. 3, no. 2, p. 711, 2012.
- [9] Z. Rafiee, M. Rafiee, and M. R. Aghamohammadi, "A new control strategy based on reference values changing for enhancing LVRT capability of DFIG in wind farm," *International Journal of Renewable Energy Research (IJRER)*, vol. 9, no. 4, pp. 1626–1637, 2019.
- [10] X. Liu, Y. Han, and C. Wang, "Second-order sliding mode control for power optimisation of DFIG-based variable speed wind turbine," *IET Renewable Power Generation*, vol. 11, no. 2, pp. 408–418, 2017.
- [11] M. Darabian and A. Jalilvand, "Predictive control strategy to improve stability of DFIG-based wind generation connected to a large-scale power system," *International Transactions on Electrical Energy Systems*, vol. 27, no. 5, Article ID e2300, 2017.
- [12] X. Yuan, H. Sun, J. Wen, L. Naihu, Y. Meiqi, and Y. Liangzhong, "DFIG control design based on internal model controller," in *Proceedings of the 2010 China International Conference on Electricity Distribution (CICED)*, IEEE, Nanjing, China, pp. 1–6, September 2010.
- [13] S. Bayhan, O. Ellabban, and H. Abu-Rub, "Sensorless model predictive control scheme of wind-driven doubly fed induction generator in dc microgrid," *IET Renewable Power Generation*, vol. 10, no. 4, pp. 514–521, 2016.
- [14] M. I. Martinez, G. Tapia, A. Susperregui, and H. Camblong, "Sliding-mode control for DFIG rotor- and grid-side converters under unbalanced and harmonically distorted grid voltage," *IEEE Transactions on Energy Conversion*, vol. 27, no. 2, pp. 328–339, 2012.
- [15] L. Djilali, E. N. Sanchez, and M. Belkheiri, "Real-time implementation of sliding-mode field-oriented control for a DFIG-based wind turbine," *International Transactions on Electrical Energy Systems*, vol. 28, no. 5, Article ID e2539, 2018.
- [16] G. Sarwar Kaloi, J. Wang, and M. Hussain Baloch, "Dynamic modeling and control of DFIG for wind energy conversion system using feedback linearization," *Journal of Electrical Engineering and Technology*, vol. 11, no. 5, pp. 1137–1146, 2016.
- [17] A. Medjber, A. Guessoum, H. Belmili, and A. Mellit, "New neural network and fuzzy logic controllers to monitor maximum power for wind energy conversion system," *Energy*, vol. 106, pp. 137–146, 2016.
- [18] J. Han, "From PID to active disturbance rejection control," *IEEE Transactions on Industrial Electronics*, vol. 56, no. 3, pp. 900–906, 2009.
- [19] G. Herbst, "Practical active disturbance rejection control: bumpless transfer, rate limitation, and incremental algorithm," *IEEE Transactions on Industrial Electronics*, vol. 63, no. 3, pp. 1754–1762, 2016.
- [20] R. Madoński, M. Nowicki, and P. Herman, "Application of active disturbance rejection controller to water supply system," in *Proceedings of the 33rd Chinese Control Conference*, IEEE, Nanjing, China, pp. 4401–4405, July 2014.
- [21] H. Laghridat, A. Essadki, and T. Nasser, "Comparative analysis between PI and linear-ADRC control of a grid connected variable speed wind energy conversion system based on a squirrel cage induction generator," *Mathematical Problems in Engineering*, vol. 2019, Article ID 8527183, 16 pages, 2019.

- [22] I. Aboudrar, S. El Hani, H. Mediouni, and A. Aghmadi, "Active disturbance rejection control of shunt active power filter based on PQ theory," in *Recent Advances in Electrical and Information Technologies for Sustainable Development*, Springer, Cham, Switzerland, 2019.
- [23] I. Aboudrar, S. El Hani, H. Mediouni, A. Aghmad, and M. S. Heyine, "Robust control of three phase grid connected PV system based on ADRC and fuzzy," in *Proceedings of the 2018 6th International Renewable and Sustainable Energy Conference (IRSEC)*, IEEE, Rabat, Morocco, pp. 1–6, December 2018.
- [24] M. Chakib, A. Essadki, and T. Nasser, "Robust ADRC control of a doubly fed induction generator based wind energy conversion system," in *Proceedings of the International Conference on Electronic Engineering and Renewable Energy*, Springer, Singapore, pp. 359–368, April 2018.
- [25] M. Arbaoui, A. Essadki, I. Kharchouf, and T. Nasser, "A new robust control by active disturbance rejection control applied on wind turbine system based on doubly fed induction generator DFIG," in *Proceedings of the 2017 International Renewable and Sustainable Energy Conference (IRSEC)*, IEEE, Tangier, Morocco, pp. 1–6, December 2017.
- [26] I. Aboudrar, S. El Hani, H. Mediouni, and A. Aghmadi, "Modeling and robust control of a grid connected direct driven PMSG wind turbine by ADRC," *Advances in Electrical and Electronic Engineering*, vol. 16, no. 4, pp. 402–413, 2018.
- [27] H. Laghradat, A. Essadkil, M. Annoukoubil, and T. Nasser, "Linear active disturbance rejection control (LADRC) of a variable speed wind energy conversion system using a DFI-generator," in *Proceedings of the 2018 6th International Renewable and Sustainable Energy Conference (IRSEC)*, IEEE, Rabat, Morocco, pp. 1–6, December 2018.